Waste heat recovery using thermally responsive ionic liquids through TiO 2 nanopore and macroscopic membranes

Marc Pascual, Nicolas Chapuis, Soufiane Abdelghani-Idrissi, Marie-Caroline Jullien, Alessandro Siria, Lydéric Bocquet

Journal Name

ARTICLE TYPE

Cite this: DOI: 00.0000/xxxxxxxxxx

Waste heat recovery using thermally responsive ionic liquids through TiO2 nanopore and macroscopic membranes

Marc Pascual,[a‡] Nicolas Chapuis,[a‡] Soufiane Abdelghani-Idrissi,[a] Marie-Caroline Jullien,[b] Alessandro Siria,[a] and Lydéric Bocquet[a]

Received Date
Accepted Date

DOI: 00.0000/xxxxxxxxxx

Waste heat is the untapped heat produced by a thermodynamic process. It is usually released in the surrounding environment without any valorization. But recently, industrial waste heat has been identified as a promising energy source and many techniques have been proposed for its recovery. In this paper we present a method to convert low temperature waste heat ($T < 100^o$C) into salinity gradients, from which osmotic power is harvested across a nanoporous membrane. The heat is used to trigger the phase separation of a lower critical solution temperature (LCST) water-ionic liquid mixture. The two phases, of different salt concentration, are fed in two reservoirs separated by a membrane with nanopores $\approx 30-100$ nm in diameter. An osmotic electric current is measured across the membrane for various concentration ratio and pH, the origin of which is shown to be a diffusio-osmotic (DO) process occurring at the TiO_2 pore surface. The power density across the nanoporous TiO_2 membrane is found to reach 7 $W.m^{-2}$. This opens up new avenues for the harvesting of waste-heat using nanoporous membranes and ionic liquids in a closed-loop configuration.

1 Introduction

Access to cheap and low carbon footprint sources of energy has become a key challenge for our modern society[1]. Several opportunities for renewable energy production are now available, ranging from solar and wind to water-based power-generation, all of them contributing to the required mix of energy sources[1,2]. Among others, waste heat recovery technologies have generated a growing interest over the last two decades. Their aim is the harvesting of residual heats generated by industrial processes such as nuclear power plants, foundries or vehicle engines. Several possibilities exist to do so. Originally and most extensively studied, organic rankine cycles (ORC) and solid-state thermoelectrics (Seebeck effect) suffer from their low power density and the prohibitive cost of their materials, which prevent their large-scale deployment[3]. Moreover, recovering energy using these techniques has clear downsides, such as environmentally harmful refrigerants, limitation of downsizing in ORC, low efficiency and poor form factor in thermoelectric element[4].

The most promising techniques are now based on a working fluid, which is used either directly to produce electricity or via a salinity gradient. For the directs ones, thermoelectrochemicals cells are developed, which use a temperature-dependent redox couple at the electrodes. For the highest Carnot efficiency known, Im *et al*. report a surfacic power of $6,6$ $W.m^{-2}$ [5]. Another technique, the thermally regenerative electrochemical cycle which was originally designed for high temperatures, now demonstrates Carnot efficiencies up to 40% at lower temperatures (below a hundred degrees Celsius)[6].

Concerning the techniques using a salinity gradient, they are based on osmotic power such as pressure retarded osmosis (PRO), reverse electrodialysis (RED) and diffusio-osmosis current generation (DO), originally studied and developed for harvesting the energy from the salinity gradient between sea water and rivers. The denomination of osmotic power refers to the free energy that can be extracted from the difference in salinity between two solutions, based on the entropy of mixing of the salt[7]. For a mixture of sea and fresh water, nearly 3 kJ per litre can be typically harvested with this technique[2]. However, beyond their 'blue energy' application, such processes find promising applications to harvest waste heat energy. PRO technique was shown to be efficient in harvesting the energy[8], with the PRO efficiency increasing when submitted to external heat since osmotic pressure increases with temperature[9]. However this process suffers from fouling, induced by the inherent selectivity needed to perform PRO exper-

[a] *Laboratoire de Physique de l'Ecole Normale Supérieure, ENS, Universite PSL, CNRS, Sorbonne Université, F-75005 Paris, France*
[b] *Université Rennes 1, CNRS, IPR (Institut de Physique de Rennes) - UMR 6251, F-35000 Rennes, France*
‡ These authors contributed equally to this work

iments[10]. The principle of waste heat recovery using RED and DO is to use the heat losses as an energy source to separate a thermoresponsive liquid into several phases. As the temperature is lowered to ambient temperature, the two phases recombine and it is possible to harvest this mixing energy. Strategies are based on LCST (lower critical solution temperature) mixtures to induce a salinity gradient under mild conditions with a temperature around 60°C[11,12]. Examples of water-based LCST systems consist of hydrogels[13,14] or ionic liquids (IL)[15,16]. Recent work showed that thermolytic solutions can be used for waste heat recovery using RED process[4], this study shows performances in the range of 0.8 $W.m^{-2}$, using ammonium bicarbonate. Overall, one key bottleneck of this energy conversion technology is the limited energy efficiency of the conventional methods[17]. Therefore the state-of-the-art efficiency of current technologies is still too low to make these sources of energy industrially viable processes at large scales.[2].

On the other hand, using DO to harvest mixing energy has several benefits compared to conventional processes. First, DO is a surface induced phenomenon (at the surface of the pores of the membrane), and does not require full selectivity and thus no osmotic pressure is built across the membrane. This gives the benefit of avoiding the need of sub-nano pores structures of the membrane, which are complex and expensive to manufacture. Moreover, as the membranes are not selective, they are not subjected to osmotic pressure which usually induce high mechanical stresses on the material. Membrane materials are usually designed in order to sustain these high stresses, which restricts the materials selection and complicates manufacturing. Last, the PRO process requires industrial equipments which can withstands high pressures, and this results in a more complex and expansive setup, associated with higher development/operational costs. Avoiding the need of selectivity should also lead to reduce membrane fouling which is one of the biggest limitation of conventional techniques. Overall DO mechanisms and its consequences allow broadening the range of materials for membrane and their structure, with less constraints, and possibly cheaper materials. This is a key advantage to explore.

In this context, recent works using nanomaterials for DO current generation have unveiled new perspectives in this domain, with proof of concepts for high energy conversion[7,18,19]. In[20], the osmotic energy production using boron-nitride nanotubes (BNNT) as membrane was shown to reach kilo-Watts per square meter, which is more than two orders of magnitude larger than what has been reached so far with classical membranes and nanopores[7,21]. These performances were even surpassed in recent experiments using thin films of MoS_2, with an osmotic power reaching megaWatts per square meter[22] at the single pore level. The origin of such performance is a combination of several factors. First, it was shown in the experiments using single BNNT nanotube that the electric current is generated via a diffusio-osmotic mechanism under salinity gradients, rather than based on a complete ion selectivity as in RED or PRO. Diffusio-osmosis is a surface driven mechanism which takes its origin in a local osmotic pressure gradient occurring within the first few nanometers from the surface of the pores[23–27]. The surface nature of the diffusio-osmotic current releases the condition for selectivity achieved by sub-nanometric pores through the membrane: for example, the diameters of the BN nanotubes in Ref.[20] were in the range of tens of nanometers. A second key ingredient for the large energy conversion measured in the BNNT membrane is a material property of the BN itself. As shown in[20], the BNNT surface exhibits a very large surface charge, rising up to -1 $C.m^{-2}$ and the generated electric current and power were shown to be directly proportional to this surface charge. In the case of the results of Ref.[22], the high power also originates in the molecular thickness of the membrane, leading to very steep salinity gradients[28,29].

These fundamental results merely offer a guideline and a blueprint to propose alternative avenues to harvest osmotic energy, based on membrane processes involving diffusio-osmotic mechanisms across highly charged nanoporous materials. In this context, we show that a water-ionic liquid (IL) LCST mixture coupled with a titanium dioxide (TiO_2) nanoporous membrane could be an interesting process to harvest waste heat. Titanium dioxide is a very interesting material due to its high surface charge[30,31], up to -0.2 $C.m^{-2}$, making it a good candidate for the production of osmotic energy conversion membranes[32]. Furthermore, it can be coated on various substrates such as glass, fibres, stainless steel and other inorganic materials[33,34], and is available at a large-scale. However, the ultra-high performance of DO at nanoscale are known to decrease when going from single nanopores to many pores and membranes. Reservoir and interfacial resistances as well as concentration polarization effects are usually invoked as a limiting mechanism in the scale-up[35,36]. In this context, we propose a study comparing different scales going from single nanopore to multi-pores and commercial membrane. Our work is focused on the feasibility of waste heat harvesting using DO currents in IL-water mixtures. We thus describe an experimental investigation of ionic liquid ions transport through various TiO_2 nanoporous membranes, with (i) a unique nanopore, (ii) multiple nanopores designed with controlled crystallinity by Atomic Layer Deposition (ALD) and (iii) through a commercial, macroscopic TiO_2 nanoporous membrane. This allows (i) to characterize exhaustively the properties of water-ionic liquid mixtures and TiO_2 as materials for osmotic energy conversion, and (ii) to assess their potential in terms of energy conversion at larger scale and make a proof-of-concept for the first steps of upscaling. A power density up to $\approx 7\ W.m^{-2}$ can be harvested under temperature gradients across a commercial TiO_2 membrane. This proof of concept paves the way for novel waste heat recovery applications. This first experimental scaling step -from single nanopore to lab-scale- underlines the potential of such systems, which presents several benefits compared to conventional techniques. In addition to their promising performance, such systems could potentially be used in a wide range of industrial applications, where energy losses due to dissipated heat represent a significant industrial cost. Moreover, the use of IL mixture allows also the recovery of wasted heat at non-excessive temperature ($\sim 50°C$), which is usually not efficient for conventional processes.

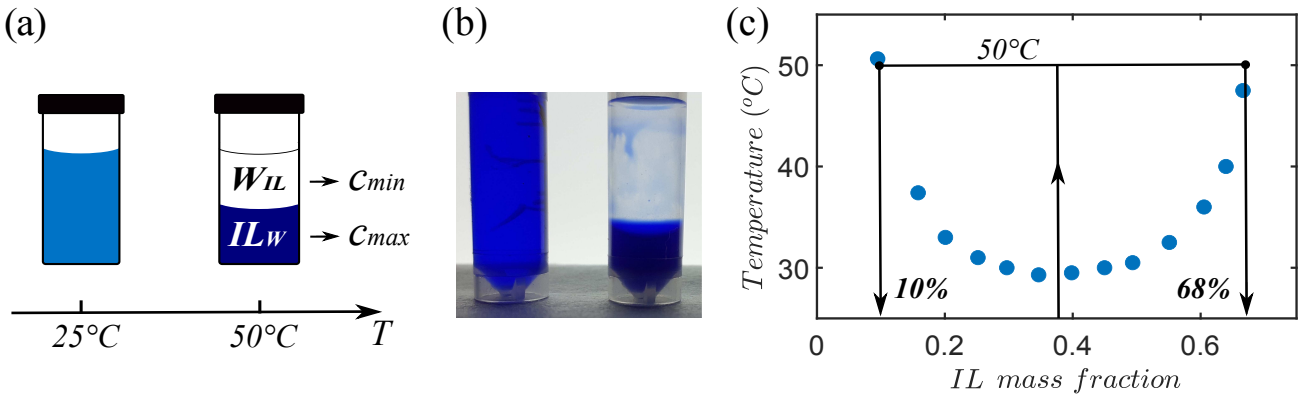

Fig. 1 (a) Equilibrium state of the binary mixture at 25°C and 50°C. The IL-rich phase is denser than the water-rich phase. The IL is dyed in blue for sake of clarity. (b) Picture of the binary mixture before (left) and after (right) phase separation. (c) Phase diagram of the water-IL mixture. Upon heating, the phase separation generates two phases of different salinities. The critical point of this LCST system is at 35 wt% in IL and 29.5°C.

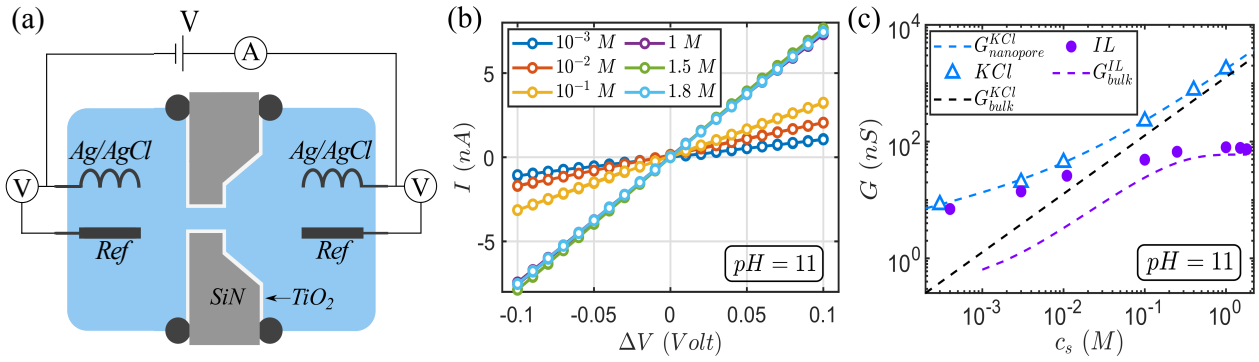

Fig. 2 (a) Sketch of the fluidic cell connected to the amplifier Axopatch 200B via Ag/AgCl electrodes. A potentiostat with a 4-electrodes channel (Biologic SP-200) allows to add a reference electrode (PINEresearch LowProfile Reference Electrode) . The pore is covered by a ≈ 5 nm thick TiO_2 layer. (b) Current versus voltage curves for an individual TiO_2 nanopore at different concentrations in IL, pH 11. The pore length is 500 nm and its diameter is 190 nm. (c) Experimental conductance values for a TiO_2 nanopore filled with KCl (triangles) or IL solutions (full circles) at pH=11. The blue dashed line is given by equation 1. The black dashed line gives the bulk conductance of the pore filled with KCl solution. The purple dashed line is given by equation 1 with $\ell_{Du} = 0$ (no surface charge contribution), it gives the bulk conductance of the pore filled with IL solution.

2 Material & Methods

In this paper, we explore mainly two types of systems: on the one hand, single or multiple nanopores pierced in SiN membranes, then coated with a TiO_2 layer using atomic layer deposition (ALD) process; and on the other hand a macroscopic TiO_2 membrane.

First, silicon nitride (SiN) membranes (Norcada), pierced with 1 or 900 (30×30) nanopores, are coated with Al_2O_3 and TiO_2 by atomic layer deposition (ALD) process. Al_2O_3 is first deposited on the SiN membrane and helps with the adhesion of the TiO_2 layer. The membranes size is 0.5×0.5 mm; they are 500 nm in thickness and fixed on a 7.5×7.5 mm frame. The pore diameter obtained after ALD coating is around 190 nm.

Al_2O_3 ultrathin films of 3 nm were deposited using a commercial ALD system (*Savannah* Veeco). Al_2O_3 was obtained by alternating exposures of TMA (trimethylaluminium, Sigma Aldrich) and H_2O at 150°C with the following cycle times: 0.15 s pulse (TMA), 30 s exposure, and 40 s purge with dry nitrogen and a 0.1 s pulse (H2O), 30 s exposure and 40 s purge. The growth per cycle (GPC) was reported elsewhere to be 1 angstrom/cycle for Al_2O_3. We note here that Al_2O_3 could not be directly used for the osmotic energy purpose, due to the low surface charge of Al_2O_3 [37]. Then, after Al_2O_3 ALD deposition, all samples were functionalized by TiO_2. A thin layer of TiO_2 (5 to 10 nm) was deposited over the Al_2O_3 ALD surface. Tetrakis(dimethylamino)titanium (TDMAT, Sigma Aldrich) and H_2O were used as precursor for TiO_2 deposition at 150°C using the following cycle: 0.2 s pulse (TDMAT), 30 s exposure, and 40 s purge with dry nitrogen and a 0.1 s pulse (H_2O), 30 s exposure and 60 s purge. The growth per cycle (GPC) was reported at 130°C to be 0.7 angstrom/cycle. We note here that the conformal coating of ALD on high aspect ratio pores has been widely studied in the literature [38] and the conformal coating inside the single and multiple nanopores membranes by Al_2O_3 nanolaminates as well as by TiO_2 has been demonstrated elsewhere [39,40]. Subsequent to ALD coating, the samples are annealed in air at 500°C for 3 h in a muffle furnace. The final characteristics of the pores are: diameter $D \approx 190$ nm and thickness $L \approx 500$ nm. The annealed pores are expected to be covered by anatase crystalline TiO_2 [32].

Second, we explore alternative macroscopic TiO_2 nanoporous membranes (Fraunhofer IKTS), usually used for ultrafiltration. The support (thickness $\approx$ 1 mm) gathers several intermediate

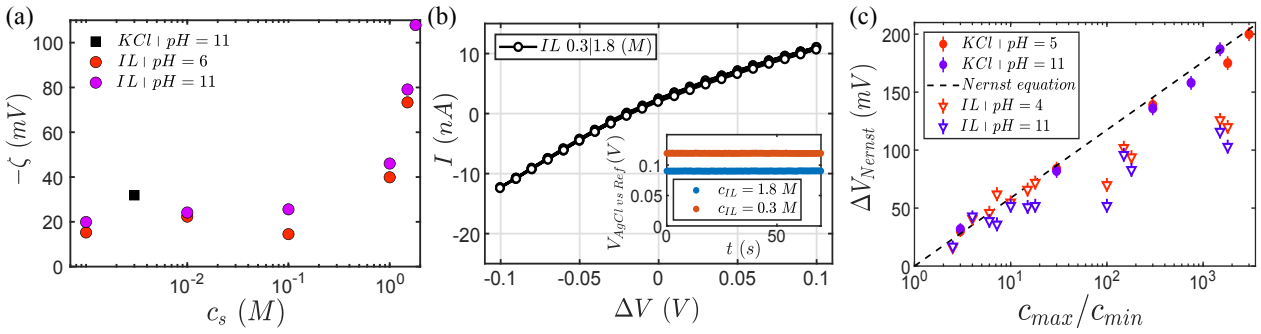

Fig. 3 (a) Zeta potential deduced from streaming currents measurements. The strong increase at high concentrations is due to the water-IL mixture viscosity increase. (b) Current vs voltage for a TiO_2 nanopore with concentrations in IL of 0.3 and 1.8 M on each side of the membrane, at pH 11. Inset: Ag/AgCl electrode potential in each reservoir vs the reference electrode introduced in the reservoir. (c) Nernst potential measured between the two Ag/AgCl electrodes versus the concentration ratio c_{max}/c_{min}, for KCl and IL salts, at pH 4 and 11. The dotted line gives the prediction of the (Nernst) equation 3.

porous layers made on TiO_2 with 5 μm pores size. The top layer (thickness $\approx 5-10\ \mu m$) is also in TiO_2 but with an average 30 nm pore size. This value, measured by mercury intrusion measurements by Fraunhofer, is consistent with our SEM images. We assemble this macroscopic membrane on a Silicon nitride (SiN) membrane (Norcada) without TiO_2 with a window of 10 μm^2 so that the active surface of TiO_2 membrane used to study the transport is also 10 μm^2. We have examined its structure in the SEM, see Fig. 6(a) and Fig. S7 of the supplemental materials. By imaging the surface it provides an estimate of the surface density of pores of $\approx$ 50-100pores.μm^{-2}.

The thermosensitive binary system of interest is a mixture of MilliQ water with the ionic liquid tetrabutylphosphonium trifluoroacetate ($P_{4444}CF_3CO_2$)[41,42], already used in different applications[11,12,15]. This system is known as a Lower Critical Solution Temperature (LCST) binary solution, *i.e.* it phase separates above a critical temperature to yield two distinct phases, as shown on Fig. 1(a),(b).

The phase rich in IL has a higher salinity than the water-rich phase, hence those two phases are used to generate the salinity gradient across the nanopores. Fig. 1(c) displays the phase diagram of this binary mixture with the critical point at 29.5^{o}C and 35 wt% in IL. For a mixture heated at 50^{o}C, the two phases are respectively 10 wt% (0.25 M) and 68 wt % (1.8 M) in IL, providing a salt concentration ratio $c_{max}/c_{min} = 7.2$. An immediate consequence of this phase diagram is that this type of IL mixture undergoes phase separation at relatively mild temperatures, and this separation process can be reversed when going back to ambient temperature. In our work, we use this (de)mixing process to show that waste heat can be used to induce phase separation in the IL, which will then recombine and produce an electric DO current at lower temperature. The phase diagram shown in Fig. 1(c) shows that the concentrations of the two phases are governed by the temperature used for heating, thus we studied several temperature inputs which translates into several concentration ratios, ranging typically from 1 to 10. In order to investigate the behavior of this type of system at higher concentration gradients, we also diluted the water rich phase in order to obtain concentration ratios in IL up to 2000.

Ion transport measurements were performed in a home-built flow cell with the $TiO2$ nanopore(s) membrane or the macroscopic TiO_2 membrane separating two reservoirs. The silicon nitride membrane used to support the TiO_2 nanopores defines the active surface of the macroscopic membrane and fits in a 7.5×7.5 mm groove specifically made in the cell. Then it is sealed on both sides with two O-rings[43]. A sketch of the sealed nanopore is shown in Fig. 2(a). The two reservoirs contain solutions of IL in MilliQ water at various concentrations c_s from 10^{-3} M to 1.8 M. The pH of the solutions ranges from 4 to 11 and is controlled by adding proper amounts of $P_{4444}OH$ (for pH $>$ 7) or CF_3CO_2H (for pH $<$ 7). We use Ag/AgCl electrodes (silver wires with a diameter of 0.5 mm), connected to an amplifier Axopatch 200B or a SP-200 potentiostat from Biologic, to impose a voltage and to measure the ionic current across the TiO_2 nanopore, with a precision in the picoampere range. Typical imposed voltage ranges from -0.1 V to 0.1 V.

Additional low profile reference electrodes (RRPEAGCL2, PineResearch) are inserted in both reservoirs to monitor the electrode potential of the homemade Ag/AgCl wire electrodes in ionic liquid solutions before and after the measurements. This 4-electrodes set-up allows to isolate the electric potential of each electrodes, without measuring the membrane contribution. This set-up is therefore useful to measure the Nernst potentials of the electrodes under salinity gradients. The electrodes potentials of our homemade Ag/AgCl electrodes is expected to follow the Nernst equation prediction when immersed in KCl solutions, however with IL solutions their value is unknown and needs to be recorded in order to isolate the Nernst contributions from the osmotic currents. The experimental determination of the electrode potential as a function of IL concentration can be found in the supplementary material Fig. S10.

3 Results

3.1 Caracterisation of individual nanopore

Firstly, we examine a single nanopore of TiO_2. In Fig. 2(b) we show a representative set of voltage-current curves for this individual nanopore obtained for different concentrations of IL from 10^{-3} M to 1.8 M at pH 11. These I-V curves are studied in or-

der to characterize and understand the nanopore behavior, especially the presence of a surface conductance. The electric conductance is defined as $G = I/\Delta V$ and obtained from a linear fit of the voltage-current curves. The experimental conductance values for IL and KCl solutions are shown in Fig. 2(c) as a function of the salt concentration.

At small salt concentration the conductance exhibits a strong deviation from the bulk linear law for both KCl and IL electrolytes, which is a signature of a surface conductance due to the presence of surface charge[24]. One specific feature is the low aspect ratio of the nanopores, which exhibit a diameter D comparable to their length L, and the electric entrance effect for the conductance has to be properly taken into account. Such effect was demonstrated experimentally and successfully modelled theoretically in Ref.[43]. The theoretical relation for the nanopore ionic conductance G, accounting for both the pore contribution and the electric entrance effect, is predicted as[43]:

$$G = \kappa_b \left[\frac{4L}{\pi D^2} \frac{1}{1+4\ell_{Du}/D} + \frac{1}{D+\ell_{Du}} \right]^{-1} \quad (1)$$

with κ_b the bulk conductivity of the electrolyte and $\ell_{Du} = \Sigma/(ec_s)$ the Dukhin length, Σ the surface charge. The above equation can be used to extract the surface charge from the conductance measurements with KCl. These data are shown in the supplementary materials (Fig. S4(b)): the extracted surface charge is then found to increase with the salt concentration as $\Sigma \propto c_s^\gamma$, with γ an exponent in the range $0.25 - 0.35$. The blue dashed line in Fig. 2(c) is accordingly a fit of the conductance using equation 1 with $\Sigma = a c_s^\gamma$. The value of the surface charge measured for the two membranes is up to -0.3 $C.m^{-2}$ for large pH values and salt concentrations, in agreement with previously reported values[30–32]. Independent measurements of zeta potential via pressure driven streaming currents, see Fig. 3(a), allow us to assess the negative sign of the surface charge, again for both KCl and IL electrolytes. Note that the rise of ζ with IL concentration echoes the viscosity increase of the solution (see Fig. S2a for the IL viscosity). Interestingly a similar behaviour for the salt concentration dependence of the surface charge was also reported for other materials, see e.g. Ref.[44] for individual carbon nanotubes. As shown in[44] and further discussed in[45,46], such scaling behaviour can be attributed to a charge regulation mechanism for the surface charge at the surface of the nanopores. A scaling analysis of the ionic transport within the non-linear Poisson-Boltzmann framework leads in the small concentration regimes to a scaling of the surface charge as $\Sigma \propto c_s^{1/3}$.

The conductance of a pore filled with IL is sensibly smaller than with KCl, this discrepency stems from the lower conductivity of the IL solutions: IL ions are bigger and less mobile than KCl ions (see Fig. S4b in the supplementary materials for the IL conductivity). The purple dashed line in Fig. 2(c) reports the pore conductance filled with IL in the absence of surface contribution. As the interaction of the IL with the surface is not well understood yet, we remove the surface charge contribution in the fit by setting $\ell_{Du} = 0$.

After studying IL transport under electrical polarisation, we examine IL transport under a concentration gradient. We used different salt concentrations in the range $10^{-3} - 1.8\ M$ in the two reservoirs and measured the resulting electric current for a variety of concentration ratios, c_{max}/c_{min}. The ionic current is corrected for the contribution resulting from the Nernstian potential originating in the difference of salt concentration at the two electrodes following the same procedure as in Ref.[20]. I-V curves under concentration gradient allows to extract the conductance in presence of a chemical potential drop across the membrane, which is necessary to isolate the Nernst current (see[20]). Fig. 3(b) displays the I-V curve obtained for a TiO_2 nanopore submitted to a salt gradient with 0.3 and 1.8 M in IL. The curve shows a slight rectification which is characteristic of a concentration diode[47]. The current I_0 at $\Delta V = 0$ is non-zero and is the sum of a Nernst current and an eventual difffusio-osmotic current: $I_0 = I_{Nernst} + I_{DO}$, with $I_{Nernst} = G \times \Delta V_{Nernst}$. For KCl solutions the Nernst potential difference ΔV_{Nernst} at a given concentration is given by the Nernst equation:

$$E = E^o + 0.059 \log\left(\frac{a_{ox}}{a_{red}}\right) \quad (2)$$

yielding for the following reaction $Ag + Cl^- \longleftrightarrow AgCl + e^-$ (in Volt):

$$E = 0.222 - 0.059 \log([Cl^-]) \quad (3)$$

However, for IL solutions we need to measure this Nernst potential for the Ag/AgCl electrode in each reservoir in order to get ΔV_{Nernst}. The inset in Fig. 3(b) shows the electric potential of the electrodes immersed in the IL solutions of 0.3 and 1.8 M. The values recorded for the entire IL concentration range of this study are gathered in Fig. 3(c). The Nernst potential difference is systematically smaller with the IL salt than with KCl salt, and the pH has little effect. This trend is consistent with the osmolality measurements of the IL, showing a non-ideal behavior of the concentrated IL solutions[15]. Those values are used to estimate the Nernst contribution to the current in order to deduce the diffusio-osmotic contribution I_{DO} with IL solutions. The Nernst contribution takes its origin in the electrochemistry at faradic electrodes, such as the Ag/AgCl electrodes used here, while no Nernst contribution builds up for non-faradic, capacitive electrodes. In the former case both the Nernst and DO contributions to the current can be harvested, while in the latter (capacitive) case, only the DO current can be harvested and it is therefore important to isolate its contribution. At large scales, the type of electrode used depends of course on the way the global system is built (*e.g.* using ferri-/ferrocyanide electroactive species or carbon electrodes). In the present experiments, Ag/AgCl electrodes prove very convenient to investigate the various processes at play.

In Fig. 4 (a) & (b) we report the experimental results for the electric (ionic) current measured across a single TiO_2 nanopore as a function of the salinity ratio c_{max}/c_{min}, at pH 4 and 11. Results for concentration gradients up to 10 are obtained by heating the IL mixture, while higher ratios are obtained by diluting the IL water phase in order to investigate broadly the behavior of DO currents. Results in Fig. 4 (c) corresponds to currents that can be harvested in a realistic application (i.e. for ratios up to 10, see Fig. 1 (c))

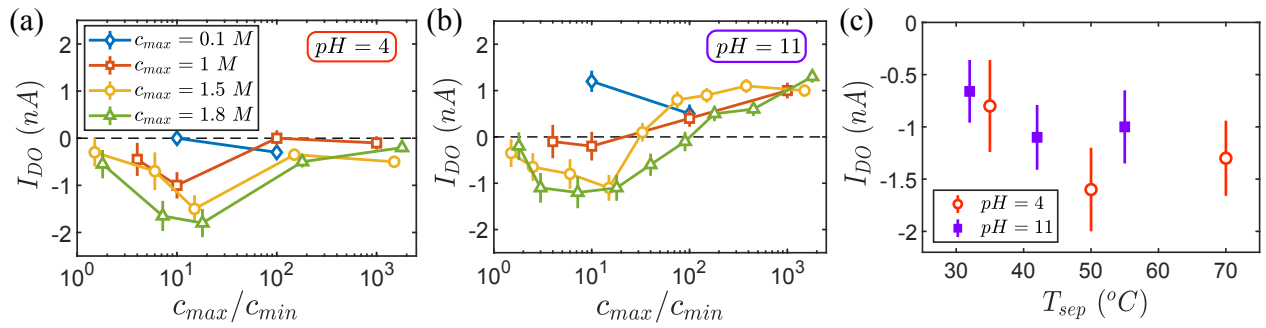

Fig. 4 (a) Diffusio-osmotic current versus the concentration ratio c_{max}/c_{min} in IL, for a TiO_2 coated nanopore at pH 4 and (b) pH 11. For (a) and (b), concentration gradients higher than 10 are obtained by dillution of IL rich water phase. (c) Diffusio-osmotic current as a function of the temperature at which the water-rich and IL-rich phases are collected after separation of the mixture. The ratio c_{max}/c_{min} is 3.4, 7.4 and 9.5 for pH 4 points and 2.5, 5.1 and 8.1 for pH 11.

As already shown for individual boron-nitride nanotubes[20], a key feature of these results is that an osmotic ionic current is generated under salinity gradients, in spite of the nanopore being fully permeable to the ions (its diameter ~ 190 nm being much larger than the ion size). This points to an origin which differs from the standard RED technology using anion and cation fully selective membranes. In spite of the membrane being permeable to ions, a diffusio-osmotic transport can be induced at the surface of the nanopore. Diffusio-osmosis is an osmotically driven, interfacial transport[23–27]: under a salinity gradient, an osmotic pressure drop is generated within the first few nanometers close to the confining surface, inside the electric Debye layer, and generates a water mass flow. This diffusio-osmotic flow however differs from the bare osmosis which requires semi-permeability of the membrane, while the pore is fully permeable to the fluid here. The diffusio-osmotic mass flow carries counter-ions within the electric Debye layer at the surface, thereby generating an electric current, I_{DO}.

For salts in water, and following the general theoretical framework presented in[20], the diffusio-osmotic water flow is typically given by a balance between interfacial osmotic pressure and the viscous stress over the Debye layer, leading *in fine* to $v_{DO} \sim \frac{\lambda_D^2}{\eta} k_B T \nabla c_\infty$ where $\lambda_D^2 \sim (8\pi \ell_B c_\infty)^{-2}$ is the Debye length, c_∞ the salt concentration in the bulk, ∇c_∞ its gradient; η is the electrolyte viscosity and $\ell_B = e^2/(4\pi\varepsilon k_B T)$ the Bjerrum length, $\ell_B = 7$ angstroms in water at room temperature. Accordingly:

$$v_{DO} \sim D_{DO} \frac{\nabla c_\infty}{c_\infty} \tag{4}$$

with $D_{DO} = k_B T/(8\pi\eta\ell_B)$ a transport coefficient, whose dimension is that of a diffusion coefficient. The electric current carried out by this flow is accordingly $I_{DO} \simeq 2\pi R\Sigma \times v_{DO}$.

From the non-monotonous trend of the I_{DO} values on Fig. 4(a)&(b), we understand that the above description shall work with simple electrolytes such as KCl but is no longer valid with concentrated solutions of IL. When $c_{max} \geq 1\ M$, $|I_{DO}|$ first increases with c_{max}/c_{min} and then decreases, even changing sign for the data at pH 11. To our knowledge, such and inversion of the diffusio-osmotic current vs concentration has not been reported experimentally up to now, although it was recently observed in simulations of KI (potassium iodide) transport along a hexagonal boron nitride surface in a concentration gradient[48]. The direction of the osmotic transport is expected to depend on the specific interactions of the solute with the surface: attractive interactions with common salts like KCl lead to a flow from high to low salt concentration, while depletion interactions with polymers lead to an opposite flow[25]. Nevertheless this classical picture does not capture every situation, and PEG or ethanol diffusio-osmotic transport led to flows from low to high concentrations despite obvious adsorption of both solutes on the walls[49]. Thus in the case of IL solutions, the sign inversion shall lie in the molecular aspects of the near-wall solute dynamics inside the nanopore and asks for a more comprehensive study. Note that this inversion of DO current appears for concentration ratios higher than the realistic applicable concentrations ratios of the IL, which are defined by the phase diagram in Fig. 1(c). Indeed, the phase diagram suggests ratios between 1 to 10 since the thermodynamics of IL separation only allow these gradients by heating the solution. Figure 4 (a,b) shows that the inversion of DO occurs out of this range of concentration ratios and should thus not be limiting in realistic applications.

To further attest the existence of diffusio-osmotic currents with IL concentration gradients, we repeat the measurements with the water-rich and IL-rich separated phases collected at various separation temperatures T_{sep}. The results are plotted in Fig. 4(c): $|I_{DO}|$ is shown to increase with T_{sep}, which is consistent with an increase of the concentration ratio c_{max}/c_{min} (see Fig. 1). The pH does not have a major effect on the magnitude of I_{DO}, as opposed to Ref.[20]. All the error bar represented in Fig. 4(c) are calculated from several experiments on the same device.

These results are consistent with theoretical expectations. Indeed, the diffusio-osmotic current can be estimated from the prediction $I_{DO} \simeq 2\pi R\Sigma \times v_{DO} \simeq (2\pi R/L)\Sigma D_{DO}(c_{max} - c_{min})/c_{mean}$, with $c_{mean} = (c_{max} + c_{min})/2$ and $\eta \simeq 3$ mPa.s the IL viscosity. In the temperature range $T_{sep} \sim 35 - 70^o$C, the phase separation leads a concentration ratio between the high and low concentration phase of typically 3.3 to 9, see Fig. 4(c). For the nanopore under investigation, with $R = 190$ nm, $L = 500$ nm, and surface

charge $\Sigma \simeq -0.2$ C.m^{-2}, one obtains a current $I_{DO} \sim 0.3-0.7$ nA, in quite good quantitative agreement with the experimental data (although slightly underestimating the measurements).

3.2 Harvested power

The previous results were demonstrated on a single TiO_2 nanopore and we now scale up the process by exploring larger scale TiO_2 membranes. As mentionned above, we consider two types of systems: (i) first a grid of 900 nanopores drilled across a membrane and further coated with TiO_2 and then (ii) a macroscopic nanoporous ceramic membrane made of bulk TiO_2 materials. In the latter, measurements were performed on a measurement window of 10 μm^2 on the nanoporous membrane, in order to compare the two sets of systems.

3.2.1 TiO_2 multipores

Let us first consider the 900 nanopore grid. In order to investigate the osmotic power, the fluidic cell is connected to an external load resistance R_L, as sketched in Fig. 5(a) and we directly measure the harvested electric power as $\mathscr{P} = I_L \times \Delta V_L = R_L I_L^2$, with I_L and ΔV_L the electric current and voltage drop across the load resistance.

In Fig. 5(b) we report the harvested power versus the load resistance. In this figure, the IL concentration contrast was obtained by heating the IL at 50^{o}C, giving a concentration ratio $c_{max}/c_{min} \sim 7$. This plot exhibits a maximum for a resistance $R_L \sim R_{multipores}$, with $R_{multipores}$ the ionic resistance of the pore; under the present conditions the multipore resistance is typically $R_{multipores} \sim 0.6$ MΩ. The multiple nanopores membrane can be represented as a (diffusio-osmotic) current generator in parallel to the pore resistance, so that, by solving the equivalent electrical circuit, one expects accordingly:

$$P(R_L) = \frac{R_L}{(R_L + R_{multipores})^2} \Delta V_{cell}^2 \tag{5}$$

with ΔV_{cell} the cell potential (which for a faradic electrode involves both the DO and Nernst contributions). The harvested power thus presents a maximum for $R_L = R_{multipores}$, in agreement with the experimental observation. The maximum value for the power measured under these conditions reaches $\mathscr{P} \approx 0.35$ nW for the 900 nanopores. This corresponds to a maximum power density of ≈ 5 $W.m^{-2}$ for this specific concentration ratio, see Fig. 5(c).

3.2.2 TiO_2 membrane

We now turn to the macroscopic ceramic membrane of TiO_2. We first characterized the membrane functional specificities (porosity, surface charge) and details are reported in the supplementary materials. To summarize, SEM images suggest that the pores have a typical 30 nm diameter and a length in the range 5-10 μm (Fig. S7). We did also measure the electric conductance of the membrane, as well as its dependence on KCl salt concentration (Fig. S8). The concentration dependence for the conductance can be accounted for by $G_{membrane} = N \times G_1$ where G_1 follows equation 1 for a unique nanopore with diameter $D = 30$ nm and length $L = 10$ μm; N is here the estimated number of pore on the measurement window. This comparison leads to a pore density of $\sim 50-100$ $pores.\mu m^{-2}$, consistent with the SEM images, and a surface charge which varies with the salt concentration between 6.10^{-3} and 4.10^{-2} $C.m^{-2}$. We further tested the response of this membrane under KCl salt gradients (Fig. S9), confirming its electric response to salinity gradient.

We now turn to the electric response under various IL concentration gradients in order to highlight the diffusio-osmotic currents across the TiO_2 membrane. Fig. 6(a) shows the different current-voltage curves across the membrane under IL gradient. For each concentration ratio, the conductance G of the system can be obtained from the slope of the $I-\Delta V$ curve, and we also extract the current at zero-voltage, which is plotted in Fig. 6(b). Now, the diffusio-osmotic contribution is deduced by substracting the Nernst contribution to the total current. To do so, we measured independently the Nernst potential for the IL solutions at various concentration using a reference electrode, see Fig. S10. The DO current is then defined as $I_{DO} = I_{offset}(\Delta V = 0) - G \times \Delta V_{Nernst}$. The result, shown in Fig. 6(b), shows an important contribution of diffusio-osmosis to the current under a IL concentration drop across the TiO_2 membrane.

Now, in order to properly measure the harvested power, we turn to the same protocol as used for the nanopore grid: a load resistance is connected to the membrane cell and electrode, and the measured electric power $\mathscr{P} = R_L I_L^2$ versus load resistance is investigated. in Fig. 7 (a)-(b), we report the result of this procedure for a specific concentration ratio $c_{max}/c_{min} \sim 9$. This ratio corresponds to a temperature difference of about 30^oC above room temperature. It also shows the fit of these values according to equation 5. The load resistance dependence of the power follows equation 5, and we observe a maximum reached for $R_{load} = R_{membrane} = 2.4\,10^6$ Ω and $P_{max} \simeq 7\,10^{-9}$ W. Normalized by the active surface $S = 10$ μm^2, this yields a power density of $P_{surf}^{max} \simeq 7$ $W.m^{-2}$, see Fig. 7 (b). This value is consistent with those of the 900 nanopores grid.

This result confirms that the performances of the macroscopic TiO_2 membranes match those of highly controlled pores in terms of osmotic power and waste heat harvesting. A great advantage though, is that such (commercially available) membrane are already scalable, and this is a key asset in the upscaling of the process. Comparing single pore DO current in Fig. 4 with harvested power for multi-pores and commercial membrane Fig. 5 and Fig. 7 shows a decrease from 0.3 $kW.m^{-2}$ at the single pore scale (with a DO current around 1 nA) to 7 $W.m^{-2}$ for multipores and TiO_2 membrane. This decrease from the single to the many pores is expected in agreement with recent literature [35]. It is ususally attributed to reservoir and interfacial resistance as well as concentration polarization [35,36]. However, this power density of $\sim 7W.m^{-2}$ is substantial in comparison to conventional techniques performances. Moreover, a nanopore-based process, with large pore sizes, has inherent advantages as discussed previously.

As a final note, we evaluate the efficiency of the process, *i.e.* the fraction of incoming energy which the system can harvest and restitute in an electric form. To do so we calculate the thermal energy required for the IL mixture separation and compare it to the electrical energy produced by the nanoporous membrane. The typical mass of IL mixture contained in the reservoirs is 1 g,

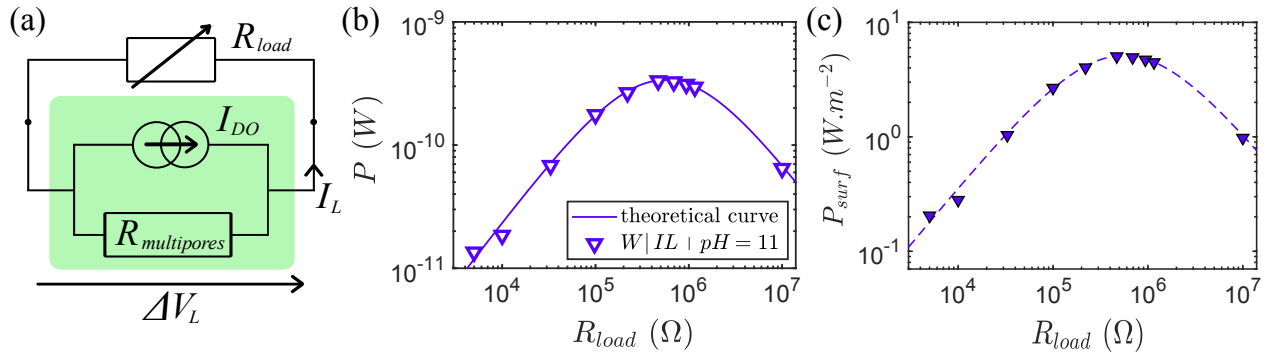

Fig. 5 Multipore results: (a) Sketch of the osmotic power measurement: a load resistance R_{load} is connected to the cell holding the nanopores membrane, represented as an ideal current generator in parallel to a pore ionic resistance. For a faradic electrode, a Nernst contribution to the potential builds up and the cell potential $\Delta V_{cell} = R_{multipores} I_L$ is the sum of the DO and the Nernst contributions. (b) Power generated by the TiO_2 coated multipores for a mixture of pH 11 heated at 50^{o}C. This corresponds to a concentration ratio $c_{max}/c_{min} \sim 7$. The fit is obtained with $R_{multipores} = 5.6\ 10^5\ \Omega$ and $\Delta V_L = 28$ mV. (c) Power density for the same sample than in (b) obtained by normalizing the measured generated power by the total surface of the 30×30 pore array.

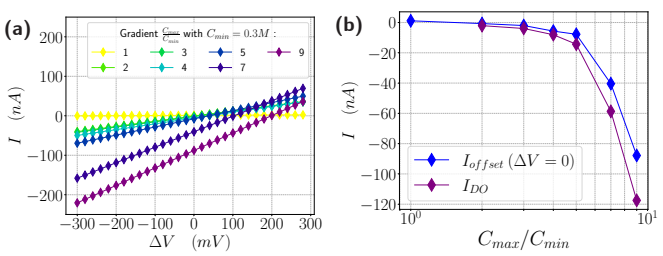

Fig. 6 Electric response of the TiO_2 membrane under IL concentration gradients: (a) Current-Voltage curves for IL under concentration gradient varying from 1 to 9. (b) Diffusio-osmotic contribution to the current across the TiO_2 membrane. The current at zero-voltage is shown versus IL concentration gradient (blue symbols). Substracting the Nernst contribution (measured independently), we deduce the diffusio-osmotic current (purple symbols).

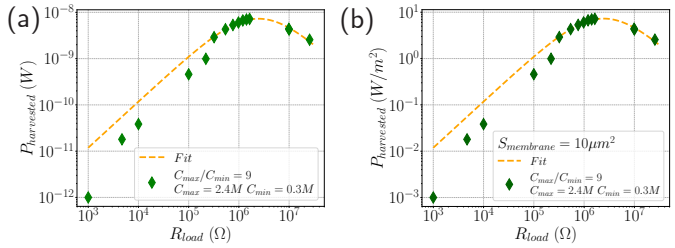

Fig. 7 Osmotic power across the TiO_2 Membrane:(a) Harvested power produced through the membrane under a IL concentration gradient of 9. We measure the current passing through the load resistance connected to the cell. (b) Harvested surface power density. The maximum value reaches 7.2 $W.m^{-2}$ for $R_{load} = 2.40\ M\Omega$.

and to raise its temperature from ambient 25^{o}C to 50^{o}C we provide $\Delta U_{thermal} = c_p \times \Delta T \approx 105$ J, with $c_p = 4.182$ J.K^{-1} the heat capacity for 1 g of water. Note here that the phase separation latent heat of mixture is ≈ 2 J per gram, *i.e.* small compared to the 105 $J.g^{-1}$ needed to heat the mixture. The osmotic energy generated by the membrane can be estimated by multiplying its power $\mathscr{P}$ with the characteristic time for the osmotic current to fade away because of complete mixing in both reservoirs $\tau \sim 1000$ s.L$^{-1} \times 10^{-3}$ L ~ 1 s. Finally we obtain $\Delta U_{osmotic} = \mathscr{P} \times \tau \approx 5$ J. The ratio $\Delta U_{osmotic}/\Delta U_{thermal} \approx 0.05$ confers an operating efficiency of $\approx 5\%$ in the present process, which is more than half the Carnot efficiency $\eta = 1 - T_{cold}/T_{hot} \approx 0.08$.

Overall, these performances shows up the potential application of harvesting waste heat using DO of IL mixture through commercial membranes. These new results highlights new opportunities for industrial reduction of energy losses, with several new benefits compared to conventional processes. In order to investigate these potential applications industrially, a larger scale-up work is now necessary, and constitutes the outlook of this experimental proof-of-concept.

4 Conclusion

In this paper, we have shown that IL-water mixtures coupled to nanoporous TiO_2 membranes allow for an effective waste heat recovery by osmotic energy conversion under salinity gradients. We report power densities reaching $\mathscr{P} \sim 7$ W.m^{-2} over commercial membranes. This value similar to typical performance reached by the state-of-the-art PRO and RED technologies with conventionnal salts. Moreover the efficiency of the cycle is estimated to be 5%. The process offers the advantages inherent to DO current, as it does not require sub-nano porosity of the membrane, and is not subjected to mechanical pressures. This opens up the range of materials as membranes for harvesting this type of energy.

Such performance results from the combination of two key features: (i) the specific material properties of TiO_2, which exhibits high surface charge; (ii) the diffusio-osmotic origin of the osmotic current. The latter is an interfacial transport mechanism occurring at the surface of the nanopores. This mechanism is demonstrated here for nanopores < 200 nm in diameter and therefore does not require highly selective membranes with subnanometric confinements, as usually for PRO and RED. Besides, the sign of the diffusio-osmotic current for IL solutions is found to vary with the IL concentration and this exotic behavior calls for more

detailed investigation.

To reach these conclusions, we performed a set of experiments combining (i) single nanopore measurements which allows for detailed investigation of IL transport on the one hand; and (ii) a first proof-of-concept for scalability with the demonstration of energy conversion over a commercial TiO_2 membrane. These results are highly promising since such TiO_2 membrane are already commercially available and scalable. This is a key asset in upscaling the process to harvest waste heats.

In the next steps, a closed loop device should be assembled including all processes at hand, in order to validate the performance of such systems in the context of upscaling. We note that this could take advantage of our recent work emphasizing the influence of confinement on the phase separation of such IL-water mixtures[50,51]. Another prospective route could be the use of UCST (upper critical solution temperature) mixtures, with a phase separated system at room temperature and a recombination across a nanoporous membrane at higher temperature. The higher operating temperature of the diffusio-osmotic module would lead to higher currents. These perspectives could lead to the development of realistic industrial systems for the efficient recovery of dissipated energy by waste heat in a wide range of industrial processes. Altogether our work shows that the use of new materials and new nanofluidic mechanisms offers out-of-the-box perspectives to make osmotic energy a promising renewable energy in the context of waste heat harvesting.

Conflicts of interest

There are no conflicts to declare.

Acknowledgements

LB and AS thanks Bruno Mottet and Pascal Lemélinaire for many interesting discussions. MP, MCJ and LB received financial support from Agence Nationale de la Recherche (ANR) under Grant No. ANR-18-CE09-0029.

Notes and references

1 S. Chu and A. Majumdar, *nature*, 2012, **488**, 294–303.
2 B. E. Logan and M. Elimelech, *Nature*, 2012, **488**, 313–319.
3 L. E. Bell, *Science*, 2008, **321**, 1457–1461.
4 D. H. Kim, B. H. Park, K. Kwon, L. Li and D. Kim, *Applied Energy*, 2017, **189**, 201–210.
5 H. Im, T. Kim, H. Song, J. Choi, J. S. Park, R. Ovalle-Robles, H. D. Yang, K. D. Kihm, R. H. Baughman, H. H. Lee, T. J. Kang and Y. H. Kim, *Nature communications*, 2016, **7**, 10600.
6 S. W. Lee, Y. Yang, H.-W. Lee, H. Ghasemi, D. Kraemer, G. Chen and Y. Cui, *Nature communications*, 2014, **5**, 3942.
7 A. Siria, M.-L. Bocquet and L. Bocquet, *Nature Reviews Chemistry*, 2017, **1**, 1–10.
8 D. D. Anastasio, J. T. Arena, E. A. Cole and J. R. McCutcheon, *Journal of Membrane Science*, 2015, **479**, 240–245.
9 S. J. Einarsson and B. Wu, *Science of The Total Environment*, 2021, **757**, 143731.
10 E. Nagy, I. Hegedüs, E. W. Tow and J. H. Lienhard V, *Journal of Membrane Science*, 2018, **565**, 450–462.
11 Y. Cai, W. Shen, J. Wei, T. H. Chong, R. Wang, W. B. Krantz, A. G. Fane and X. Hu, *Environmental Science: Water Research & Technology*, 2015, **1**, 341–347.
12 A. Z. Haddad, A. K. Menon, H. Kang, J. J. Urban, R. S. Prasher and R. Kostecki, *Environmental science & technology*, 2021, **55**, 3260–3269.
13 C.-H. Hsu, C. Ma, N. Bui, Z. Song, A. D. Wilson, R. Kostecki, K. M. Diederichsen, B. D. McCloskey and J. J. Urban, *ACS omega*, 2019, **4**, 4296–4303.
14 A. Inada, K. Yumiya, T. Takahashi, K. Kumagai, Y. Hashizume and H. Matsuyama, *Journal of Membrane Science*, 2019, **574**, 147–153.
15 E. Kamio, A. Takenaka, T. Takahashi and H. Matsuyama, *Journal of Membrane Science*, 2019, **570**, 93–102.
16 Y. Deguchi, N. Nakamura and H. Ohno, *Separation and Purification Technology*, 2020, **251**, 117286.
17 A. P. Straub, A. Deshmukh and M. Elimelech, *Energy & Environmental Science*, 2016, **9**, 31–48.
18 L. Bocquet, *Nature materials*, 2020, **19**, 254–256.
19 X. Tong, S. Liu, J. Crittenden and Y. Chen, *ACS nano*, 2021, **15**, 5838–5860.
20 A. Siria, P. Poncharal, A.-L. Biance, R. Fulcrand, X. Blase, S. T. Purcell and L. Bocquet, *Nature*, 2013, **494**, 455–458.
21 G. Z. Ramon, B. J. Feinberg and E. M. Hoek, *Energy & environmental science*, 2011, **4**, 4423–4434.
22 J. Feng, M. Graf, K. Liu, D. Ovchinnikov, D. Dumcenco, M. Heiranian, V. Nandigana, N. R. Aluru, A. Kis and A. Radenovic, *Nature*, 2016, **536**, 197–200.
23 A. Ajdari and L. Bocquet, *Physical review letters*, 2006, **96**, 186102.
24 L. Bocquet and E. Charlaix, *Chemical Society Reviews*, 2010, **39**, 1073–1095.
25 C. Lee, C. Cottin-Bizonne, A.-L. Biance, P. Joseph, L. Bocquet and C. Ybert, *Physical review letters*, 2014, **112**, 244501.
26 S. Marbach, H. Yoshida and L. Bocquet, *The Journal of chemical physics*, 2017, **146**, 194701.
27 S. Marbach and L. Bocquet, *Chemical Society Reviews*, 2019, **48**, 3102–3144.
28 D. J. Rankin, L. Bocquet and D. M. Huang, *The Journal of chemical physics*, 2019, **151**, 044705.
29 M. Macha, S. Marion, V. V. Nandigana and A. Radenovic, *Nature Reviews Materials*, 2019, **4**, 588–605.
30 M. K. Ridley, V. A. Hackley and M. L. Machesky, *Langmuir*, 2006, **22**, 10972–10982.
31 A. Folli, I. Pochard, A. Nonat, U. H. Jakobsen, A. M. Shepherd and D. E. Macphee, *Journal of the American Ceramic Society*, 2010, **93**, 3360–3369.
32 B. Mottet, L. Bocquet, A. Siria and M. Bechelany, *Device for producing energy by salinity gradient through titanium oxide nanofluid membranes*, 2021, US Patent 10,960,354.
33 S. G. Kumar and L. G. Devi, *The Journal of physical chemistry A*, 2011, **115**, 13211–13241.
34 M. Nasr, C. Eid, R. Habchi, P. Miele and M. Bechelany, *ChemSusChem*, 2018, **11**, 3023–3047.

35 J. Gao, X. Liu, Y. Jiang, L. Ding, L. Jiang and W. Guo, *Small*, 2019, **15**, 1804279.

36 Z. Wang, L. Wang and M. Elimelech, *Engineering*, 2022, **9**, 51–60.

37 V. Thangaraj, M. Lepoitevin, M. Smietana, E. Balanzat, M. Bechelany, J.-M. Janot, J.-J. Vasseur, S. Subramanian and S. Balme, *Microchimica Acta*, 2016, **183**, 1011–1017.

38 C. Marichy, M. Bechelany and N. Pinna, *Advanced Materials*, 2012, **24**, 1017–1032.

39 S. Balme, F. Picaud, M. Manghi, J. Palmeri, M. Bechelany, S. Cabello-Aguilar, A. Abou-Chaaya, P. Miele, E. Balanzat and J. M. Janot, *Scientific reports*, 2015, **5**, 1–14.

40 S. Schlicht, L. Assaud, M. Hansen, M. Lickleder, M. Bechelany, M. Perner and J. Bachmann, *Journal of Materials Chemistry A*, 2016, **4**, 6487–6494.

41 Y. Kohno, H. Arai, S. Saita and H. Ohno, *Australian Journal of Chemistry*, 2012, **64**, 1560–1567.

42 H. Ohno, M. Yoshizawa-Fujita and Y. Kohno, *Bulletin of the Chemical Society of Japan*, 2019, **92**, 852–868.

43 C. Lee, L. Joly, A. Siria, A.-L. Biance, R. Fulcrand and L. Bocquet, *Nano letters*, 2012, **12**, 4037–4044.

44 E. Secchi, A. Niguès, L. Jubin, A. Siria and L. Bocquet, *Physical review letters*, 2016, **116**, 154501.

45 P. Biesheuvel and M. Bazant, *Physical Review E*, 2016, **94**, 050601.

46 Y. Uematsu, R. R. Netz, L. Bocquet and D. J. Bonthuis, *The Journal of Physical Chemistry B*, 2018, **122**, 2992–2997.

47 A. R. Poggioli, A. Siria and L. Bocquet, *The journal of physical chemistry B*, 2019, **123**, 1171–1185.

48 L. Joly, R. H. Meißner, M. Iannuzzi and G. Tocci, *ACS nano*, 2021, **15**, 15249–15258.

49 C. Lee, C. Cottin-Bizonne, R. Fulcrand, L. Joly and C. Ybert, *The journal of physical chemistry letters*, 2017, **8**, 478–483.

50 M. Pascual, A. Poquet, A. Vilquin and M.-C. Jullien, *Physical Review Fluids*, 2021, **6**, 024001.

51 M. Pascual, A. Amon and M.-C. Jullien, *Physical Review Fluids*, 2021, **6**, 114203.